DOI: 10.13009/EUCASS2023-621
Aerospace Europe Conference 2023 – 10TH EUCASS – 9TH CEAS

A numerical study of resonance ignition for space propulsion systems

T. Jeremy P. Karpowski[1,†], *Federica Ferraro*[1], *Katharina Henn*[1], *Christian Bauer*[2], *Christian Hasse*[1]
[1]*Simulation of reactive Thermo-Fluid Systems, Technische Universität Darmstadt, Darmstadt, Germany*
[2] *Chair of Space Propulsion and Mobility, Technische Universität München, Munich, Germany*
[†] Corresponding author: karpowski@stfs.tu-darmstadt.de

Abstract
Resonance ignition is a promising concept for lightweight and reliable ignition of rocket engines. However, the physical processes and details are not yet fully understood. Here, numerical simulations can give insight into the experimentally inaccessible parts of the setup. To this end, an experimentally investigated model igniter is simulated with a density-based time-explicit solver based on the open-source OpenFOAM framework. The simulations are compared against the experimental data. The transition from jet regurgitant mode (JRM) to jet screech mode (JSM) is captured well. Furthermore, the heating at the cavity tip is reproduced for a wide range of geometric parameters.

1. Introduction

Our modern civilization relies on satellite infrastructure, which provides fundamental services such as navigation systems, television, and Earth observation. Moreover, for many companies, satellites are part of their business model, e.g., for providers of satellite internet like SpaceX's Starlink, or companies that evaluate customers' land via observation satellites. Consequently, the number of satellites in Earth's orbit has increased drastically in recent years. The annual increase in 2021 was around 42 %, resulting in 4,877 active satellites [1]. Due to their increasing number, the popular geosynchronous orbits are becoming crowded, necessitating satellites to leave these orbits at the end of their lifetime. Furthermore, the current popularity of CubeSats requires even more lightweight and compact propulsion solutions. Consequently, a reliable and compact ignition system is needed, which is able to operate after long periods of inactivity in space. Previously used hypergolic propellants are unfavorable due to their cost and safety concerns, especially for CubeSats, which are usually only allowed to carry inert propellants.
A resonance ignition system has been evaluated as a possible alternative for such in-orbit applications [2]. It is based on the principle of a Hartmann-Sprenger (HS) tube [3]. An underexpanded jet is axially aligned with a cylindrical or conical cavity, which is referred to as resonance tube. The gas exiting the jet is heated by repeated compression in the resonance tube. Despite early research on using HS tubes as rocket ignition systems (cf. [3, 4]), the concept is not yet used commercially [5, p. 1]. Resonance ignition has the advantage that it does not require high-voltage electrical components and has been successfully operated with both a methane/oxygen mixture [6] and a hydrogen/oxygen mixture [3].
Three different modes of operation can be distinguished for HS tubes: Jet instability mode, jet regurgitation mode (JRM), and jet screech mode (JSM) [7, p. 101]. The jet instability mode appears for low Nozzle Pressure Ratios (NPR). This mode does not result in significant heating [8, p. 653]. The JRM is characterized by the cavity periodically swallowing and expelling the fluid coming from the jet. The frequency of this mass exchange corresponds to the quarter-wavelength frequency of the tube [8, p. 653]. The mass flow entering the tube causes the formation of pressure waves propagating to the closed end of the tube. If the tube is long enough, the compression waves can collide to form a shock wave, in which case a normal shock or a shock followed by compression waves are formed. At the closed end, the compression waves and the shock are reflected. The outflow of the tube repels the underexpanded jet from the nozzle [9, p. 5]. This pushes the shock system exiting the jet towards the nozzle. The periodic compression of the gas at the cavity tip leads to an increase in temperature.
In the pioneering literature on JRM different plausible causes for the observed periodic flow cycle described above are proposed. Smith and Powell argued that a *stand-off* shock, a detached shock at the resonator mouth, is necessary to maintain resonance [10, p. 62f.]. When the detached shock is subjected to pressure instabilities upstream of the tube inlet, it oscillates and leads to the resonance process described above. [8] and [9] observed JRM in experiments without the presence of a stand-off shock, cf. [7, p. 102]. A more recent theory suggested that a low-pressure expansion wave

DOI: 10.13009/EUCASS2023-621

zone with pressure lower than the ambient pressure is needed around the tube wall at the tube's open end and a positive pressure gradient in the flow field upstream of the tube's inlet [11, p. 25]. The pressure gradient is required to allow the reflected shock coming from the tube's bottom to move outside of the tube into the nozzle jet [11, p. 25]. This shock is then reflected into an expansion fan, and this fan is amplified by the low-pressure region so that it is strong enough to move into the tube and be reflected into a shock when it arrives at the tube opening, thus maintaining the periodic flow cycle [11, p. 25f.].

The JSM is dominated by an almost normal shock oscillating between the nozzle jet and the tube inlet [8, p. 655]. This normal shock is a stand-off shock present during the entire flow cycle oscillating around its mean position with a frequency at the order of tens of kilohertz [8, 12]. The frequency is a function of the NPR and the spacing between nozzle exit and tube inlet [12, p. 102].

In experiments, the mode of operation of a cylindrical HS tube transitioned from JRM to JSM when the dimensionless nozzle tube distance s/d_n is varied while the NPR stayed constant [13, p. 822]. The JRM mode was identified by an oscillatory shock in front of the cavity, while the JRM mode was identified by the dominance of the quarter-wavelength frequency in the pressure spectrum [13, p. 822]. The mode could be identified by the dominant frequency. A dominant quarter-wavelength frequency indicates JRM, while a dominant high-frequency noise indicates JSM.

The variation of the NPR has a similar effect, as JRM is found to appear when the cavity is positioned behind a shock cell in the *zone of instability* [7]. Variation of the NPR results in expanded or contracted shock cells and therefore a shift of the *zone of instability* causing a JRM/JSM transition.

Experiments have shown that increasing the lip thickness changes the dominant frequencies occurring in an HS tube as a function of the nozzle-tube spacing s/d_n. Operation with a cavity diameter of $2d_n$ resulted in additional frequencies not present in the case of a $1.3d_n$ cavity diameter [14, p. 79f]. In particular, for some s/d_n ratios, the dominant frequency in JRM is superimposed by a second frequency that is even higher than the dominant frequency in JSM [14, p. 79f]. One interpretation of this phenomenon could be that a thicker tube lip causes JRM and JSM to occur simultaneously [15, p.144].

As the small geometric and temporal features prohibit optical access to the cavity, numerical simulations are essential to understand the processes inside the cavity leading to the temperature rise required for combustion, and to support its design and optimization. An overview of previous simulation setups found in literature is gathered in Tab. 1. All feature a 2D axisymmetric domain and employ (U)RANS methodology. Murugappan and Gutmark [13] performed

Table 1: Summary of simulations on HS tubes in literature, the order follows the publication dates, with the most recent publications at the bottom.

	Solver	**Turbulence Model**	**Wall Heat Transfer**	**Fluid**
[13]	Ansys Fluent	k-ε	Wall temperature takes into account radiative heat flux	Ideal gas
[16]	Ansys Fluent	k-ε	Coupled heat transfer	Ideal gas air
[12]	Ansys Fluent	k-ω SST	Adiabatic wall	Ideal gas air $c_p(T)$, $\mu(T)$
[15]	unknown	-	Not considered	Inviscid gas
[5]	Ansys Fluent	realizable k-ε	Coupled heat transfer	Ideal gas air
[6]	Ansys Fluent	realizable k-ε k-ω SST	Thin wall model	Ideal gas air $c_p(T)$, $\mu(T)$, $\lambda(T)$

CFD simulations of HS tubes operating in JRM. The motion of the shock structure in the JRM is discussed, but no information about the tip temperature is provided. The setup considered heat transfer by radiation on the outer wall of the tube and viscous dissipation on the inner walls of the tube. The main result is that the time spent in the expansion phase accounts for 41 % of the flow cycle, so the time spent in the inflow and outflow phases differs significantly [13, p. 816].

The results of a CFD simulation of a conical HS tube operated in JRM were validated with a corresponding experimental setup, and a conical and a cylindrical cavity were compared simulatively in [16]. Conjugated heat transfer was considered, and the wall temperature at the cavity tip was within 40 K of the experimental observation [16]. A comparison of simulations for cylindrical and conical pipe geometries showed a wall temperature lower by about 300 K for the cylindrical case [16]. This is due to significantly lower pressure oscillations at a measurement point inside the cavity, in the case of the cylindrical cavity.

In [12] the experimental setup from [17] was simulated. The operating point $s/d_n = 2.4$ and NPR = 4 was investigated. This work focuses on numerical simulations and analysis of the same experimental setup.

DOI: 10.13009/EUCASS2023-621

In [15] simulations solving for the Euler equations were carried out. Despite neglecting the diffusive and dissipative processes, a reasonable equilibrium temperature could be determined. In addition to observing the flow pattern in JRM, variations in cavity lip thickness were investigated. The transition from JRM to JSM was induced by varied lip thickness [15].

The work of Dickert [5] focuses on the design of a resonant igniter. Three different geometries are investigated (differing by opening angles, cavity entry diameter, and cavity length), whereby for the most promising geometry, the NPR is varied. The mean temperature for the limit cycle at the end of the cavity on the axis of symmetry varied between 468 K and 800 K for air.

Bauer [6] deals with the experimental and numerical investigation of resonant ignition systems. It aims to determine the heating rate for different geometric configurations of cavities from CFD simulations in order to advance the design process of such systems. For this purpose, experiments were performed to validate the simulation results for a simple nozzle-cavity setup. Later, the nozzle-cavity simulation setup is extended to a full resonant ignition system. Simulations utilizing a thin wall model yield a difference of 200 K or 20 % to the experimentally observed heating. A coupled conjugated heat transfer simulation resulted in a better comparison [6]. Both the k-ω SST turbulence model, and the k-ε model were applied to the resonance igniter simulation [6], with the k-ε model resulting in a better agreement with measurements of the JRM.

Within this context, this work aims to numerically evaluate a resonance igniter configuration that has been developed and experimentally investigated by Bauer [6, 17]. The numerical simulations are carried out with the open-source CDF solver OpenFOAM and the results are analyzed. The ability of reproducing experimentally observed pressure spectra and limit cycle temperature of an HS tube from [17] is demonstrated. Contrary to previous simulations from Bauer [6] which only ran 20 ms the current investigation simulated until the tip temperature reached a limit cycle, enabling direct comparison of the temperatures for all simulations. In this work, parameters of a thin wall model are fitted to replicate the limit cycle temperature of one nozzle tube spacing. The fit results in very good predictions of experimentally observed cavity tip temperatures over a wide range of nozzle tube spacing. Finally, the effect of the nozzle tube spacing on the system and the effect of the cavity shape is assessed.

In the following, the governing equations are first introduced. Subsequently, the physical and numerical setup is presented, and the numerical solver, as well as the deployed models, are discussed and verified. Lastly, the results are presented and evaluated by comparison with the experimental data. First, a mesh independence study is conducted. Then, the model parameters of the thin-wall model are fitted. Afterwards, the effect of nozzle tube spacing and cavity shape are analyzed.

2. Governing Equations

In this work, the fluid is solved with the Favre-average URANS approach. For the sake of brevity, the indicators for Favre-averaging are omitted. The Reynolds averaged equations can be written as

$$\frac{\partial}{\partial t}\begin{pmatrix}\varrho\\ \varrho\mathbf{u}\\ \varrho e_t\end{pmatrix} + \nabla\cdot\begin{pmatrix}\varrho\mathbf{u}\\ \varrho\mathbf{u}\otimes\mathbf{u}+p\mathbf{I}\\ (\varrho e_t + p)\,\mathbf{u}\end{pmatrix} = \begin{pmatrix}0\\ \nabla\cdot\boldsymbol{\tau}^{eff}\\ \nabla\cdot(\boldsymbol{\tau}^{eff}\cdot\mathbf{u}) + \nabla\cdot(\alpha^{eff}\nabla e)\end{pmatrix}, \tag{1}$$

where ϱ is the density, $\mathbf{u}$ the velocity vector, e_t the specific total inner energy, sum of the specific inner energy e and the kinetic energy $(e + \frac{1}{2}\mathbf{u}^2)$, p the pressure, $\mathbf{I}$ the identity tensor, $\boldsymbol{\tau}^{eff}$ the effective viscous stress tensor, which is the combination of the physical $\boldsymbol{\tau}$ and the turbulent viscosity tensor $\boldsymbol{\tau}^{turb}$, and similarly α^{eff} the effective thermal diffusivity, which also contains the physical and turbulent component. To close the equations, the ideal gas equation of state is utilized. The transport quantities, e.g., the viscosity μ are modeled with the Sutherland law [18]. The thermal diffusivity is obtained from a constant Prantl number assumption Pr$= 0.71$. The caloric equation of state is closed with a polynomial approximation

$$e(T) = \int c_v(T)\mathrm{d}T, \tag{2}$$

with the heat capacity at constant volume c_v ant the temperature T.

To account for the effect of turbulence, the realizable k-ε model [19] is utilized, which follows the Boussinesq approximation to model the Reynolds Stress tensor. Two additional equations, one for the turbulent kinetic energy k and one for the turbulent dissipation ε, need to be solved.

DOI: 10.13009/EUCASS2023-621

3. Experimental and Numerical Setup

In this work, the experimental configuration from Bauer [6] is simulated. A schematic of the setup is shown in Fig. 1-a). A nozzle with diameter d_n is pointed towards the cavity with diameter $d_{cav,i}$ at the inlet and $d_{cav,e}$ at the cavity tip. As fluid only air is considered for both the ambient and the jet emitted from the nozzle. All simulations and experiments are performed at a nozzle pressure ratio (NPR) of 4, meaning the total pressure before the nozzle is 4 bar, while the ambient has a pressure of 1 bar. The initial field, as well as the nozzle inlet, feature a temperature of 300 K. A schematic of the resulting flow field for the JRM is shown in Fig. 1-b). Due to the high NPR, the typical structures of an underexpanded jet form. For more details on underexpanded jet structures, see [20]. Contrary to free under-expanding jets, the presence of the cavity and the walls result in an oscillating position of the Mach disk. This is accompanied by inflow and outflow into the cavity. In the tube, compression waves collapse into a shock traveling into the cavity. It is reflected at the cavity tip where the periodic compression of the fluid leads to the increase in temperature required to ignite the mixture. To capture those phenomena, the setup is approximated with a numerical grid shown in Fig. 1-c). For all later plots the origin of the coordinate system is located at the symmetry axis at the nozzle outlet. The x-axis points towards the cavity.

Note that the cells are enlarged in the picture for improved visibility. The calculations are performed on a finer grid containing 125 209 cells. The geometric parameters of the domain are summarized in Tab. 2. Note that the nozzle cavity spacing s is varied throughout the study.

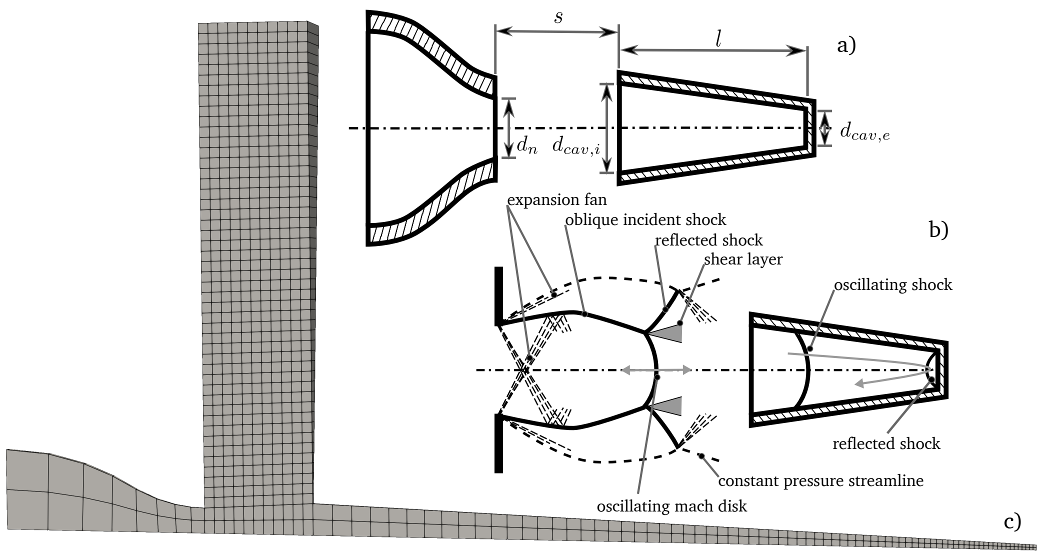

Figure 1: a) Geometric schematic of the studied configuration.
b) Physical schematic of the involved processes of the underexpanded jet and its interaction with the cavity.
c) The structure of the numerical grid with reduced cell count for better visibility. The origin of the coordinate system used in the study is located at the symmetry axis at the nozzle outlet. The x-axis points towards the cavity.

Table 2: Geometric parameters of the domain (rounded to two decimal digits).

Description	Variable	Value
length cavity	l	68.80 mm
radius cavity inlet	$0.5 \cdot d_{\text{cav,i}}$	3.12 mm
radius cavity tip	$0.5 \cdot d_{\text{cav,e}}$	0.50 mm
height environment	$0.5 \cdot d_{\text{env}} = 10 \cdot d_n$	49.95 mm
width of environment	s	variable
nozzle inlet radius	$0.5 \cdot d_{\text{n,i}}$	8.00 mm
nozzle outlet radius	$0.5 \cdot d_n$	2.50 mm
nozzle length	$0.5 \cdot l_n$	20.53 mm

At the inlet, fixed inflow conditions are prescribed. At the outlet, zero gradient conditions and a fixed pressure are set.

DOI: 10.13009/EUCASS2023-621

At the cavity walls, a wall-heat flux based on the thin wall model is calculated. All other walls are treated as adiabatic. At the inflow, a turbulent intensity of 5% is set.

4. Numerical approach

The governing equations (1) are solved utilizing an operator splitting approach. First, the left side of the equations is solved. The spatial interpolation onto the cell faces is performed with the quadratic MUSCL (Monotonic Upstream-centered Scheme for Conservation Laws) [21] reconstruction and the MinMod limiter [22]. The HLLC flux scheme [23] is utilized for the flux calculation. Time discretization is performed with a strong stability preserving forth-order Runge-Kutta method.
Afterwards, the right-hand side is solved with an implicit solver and second-order discretization in space and time. The convective change obtained from the previous step is accounted as an explicit term in the linear equation solver. Due to the potentially large implicit source terms in the k and ε equations, these equations are solved implicitly after the other equations with second-order schemes. The solver is part of the open-source blastFOAM library [24] based on the OpenFOAM framework. In Fig. 2 the solver and numerical schemes are validated against a 1D shock tube setup originally proposed by Sod [25]. Initially the tube features a high pressure zone on the left with a density of 1kg/m^3 and 0.125kg/m^3. Constant heat capacity and zero viscosity are assuemd. Good agreement between simulation and analytical solution is observed. Furthermore, the solver was validated against a 2D testcase from Lax et al. [26] and further 2D testcases from Woodward et al. [27]. Results are omitted for brevity.

To correctly predict the evolution of the temperature in the cavity, heat losses to the wall must be considered. The experimental cavity features a thin tube wall. Therefore, the heat transfer in the axial direction is assumed to be negligible. Furthermore, the main interest is the limit cycle behavior. Instead of a conjugated heat transfer simulation, the wall is always assumed to be in a steady state. Then the heat flux through the wall can be calculated from,

$$\dot{q} = \frac{1}{\frac{\delta}{\lambda} + \frac{1}{\alpha + \alpha_{\text{rad}}}} (T_{\text{iw}} - T_a) \tag{3}$$

$$\alpha_{\text{rad}} = \sigma \epsilon (T_{\text{ow}}^2 + T_a^2)(T_{\text{ow}} + T_a), \tag{4}$$

where δ is the thickness of the wall, λ the walls thermal conductivity, α the heat transfer coefficient of the wall to the ambient fluid, α_{rad} the radiative heat transfer coefficient of the wall, σ the Stefan-Boltzmann constant, ϵ surface emissivity, T_a the ambient temperature, and T_{iw} and T_{ow} the inner and the outer wall temperature, respectively. To make the solution explicit, the outer wall temperature is approximated as $T_{\text{ow}} \approx T_{\text{iw}}$ since the wall is assumed to be thin. This leaves the model with two unknown parameters α and ϵ. The other quantities are approximated from the experimental setup as $\delta \approx 0.3$ mm, $\lambda \approx 15$W/(mK), and $T_a \approx 300$ K.

In reality, the thermal mass of the metal cavity would dampen the temperature oscillation and act as a low-pass filter. Therefore, the steady-state assumption of the thin wall model results in greater oscillation amplitudes around the same averaged temperature in the limit cycle. To account for the low pass filtering effect of the solid, a moving window

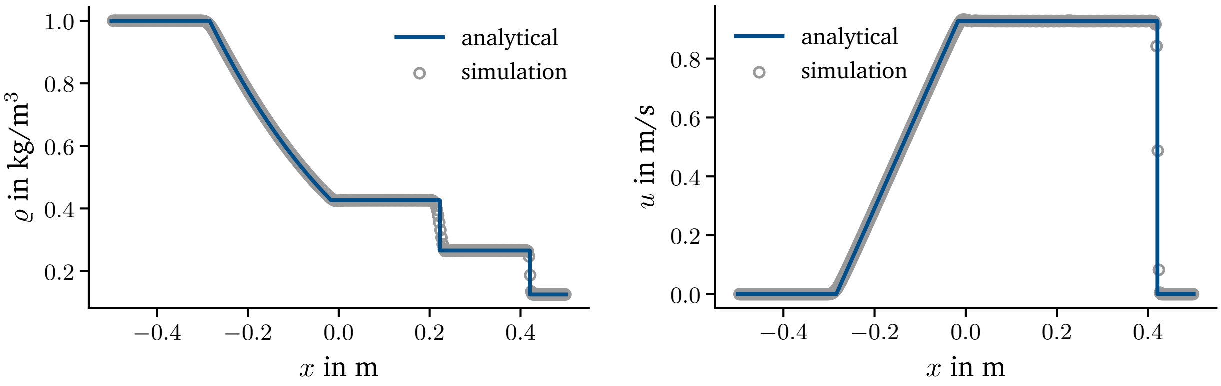

(a) Density ϱ at $t = 0.24$ s

(b) Velocity u at $t = 0.24$ s

Figure 2: Solver validation against the analytical solution of a shock tube problem originally proposed by Sod [25].

Table 3: Parameters of the grids used for the mesh study and characteristic values determined during the limit cycle.

Name	Number of cells	Limit cycle T_{tip}	Limit cycle f_{main}
coarse	80 760	787.2 K	1.9 kHz
medium	125 209	783.1 K	1.9 kHz
fine	180 147	782.3 K	1.9 kHz

filter with a width of 1 ms is applied to the T_{tip} signal. Furthermore, the tip temperature is averaged over the entire cavity tip wall.
The grid does not resolve the boundary layer completely at the cavity wall. Therefore wall functions are applied. With the contraction of the cavity, the grid reaches $y^+ \approx 1$ near the cavity tip. Therefore the wall functions are blended with a low Reynolds formulation to correctly capture those regions.
The limit cycle oscillation is detected using a confidence band for the extrema observed in the last 10 ms. If all maxima are within 15 K of each other, limit cycle oscillation is assumed. A second check based on a 15 K interval around the minima is performed as well.

5. Results

In the following sections, the results of the numerical investigations are discussed. First, a mesh independence study is performed. Afterwards, the sensitivity towards the thin wall model parameters is analyzed. The nozzle cavity spacing is varied, and the transition from the JRM to the JSM is discussed. Lastly, a conical and cylindrical cavity are compared.

5.1 Mesh independence study

The mesh independence study is carried out for a nozzle cavity spacing of $s = 2.2\,d_n$ and a NPR of 4. A JRM is expected for this spacing s, and the largest temperature increase in the cavity ΔT is observed. Thus this case is one of the most demanding in terms of grid resolution. All grids are structured and target a nearly constant cell size in front of the cavity. Cells in the cavity and nozzle adapt to the contraction of these sections as shown in Fig. 1-c). Three different grids, labeled as coarse, medium, and fine, are compared. Their size, the resulting limit cycle cavity tip temperature T_{tip} and the dominant frequency f_{main} are summarized in Tab. 3. The limit cycle values for T_{tip} differ slightly for the three configurations, while f_{main} is identical for all grids.

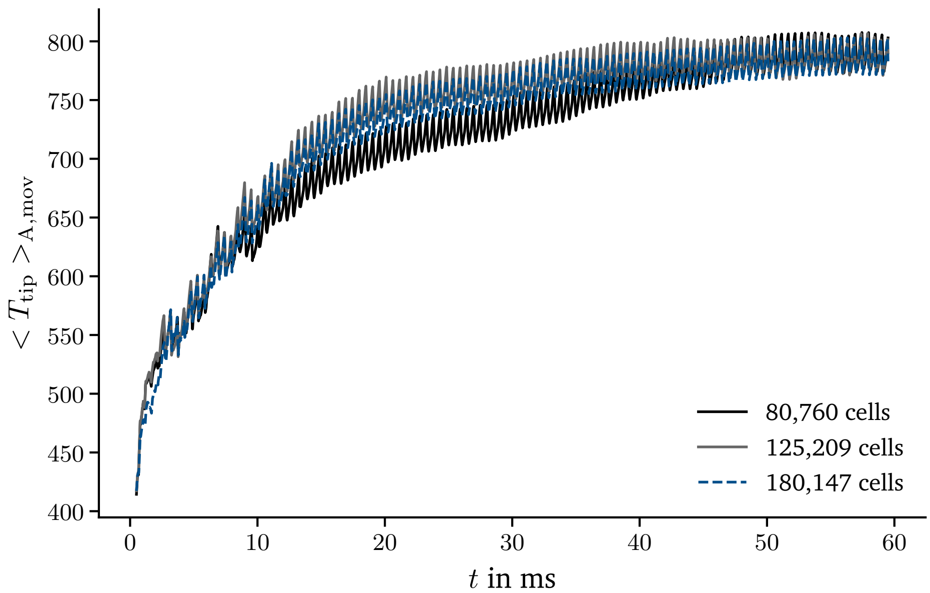

Figure 3: Moving average tip temperature for different mesh refinements.

DOI: 10.13009/EUCASS2023-621

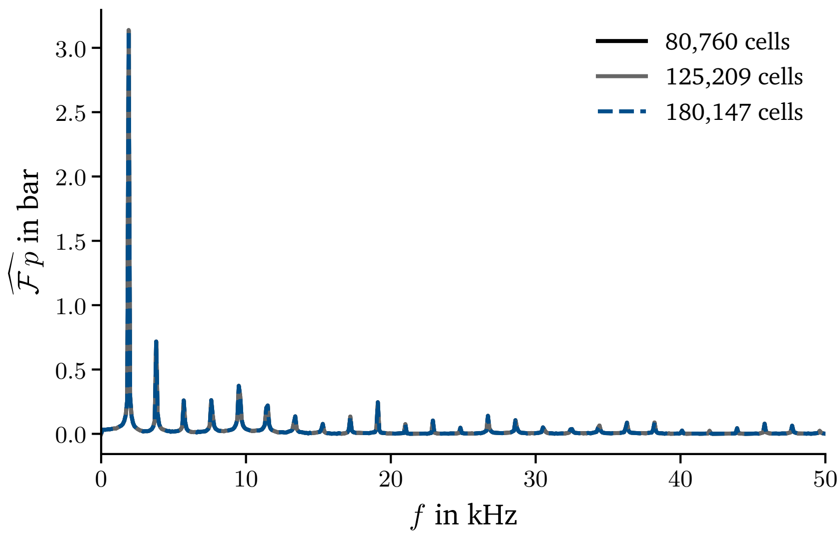

Figure 4: Scaled amplitude of the FFT of the pressure signals using different mesh sizes.

In Fig. 3, the temporal evolution of the tip temperature is shown. The moving average is applied. A similar evolution of T_{tip} is observed for all grids. However, the course grid results in lower temperatures for t between 10 ms and 40 ms. Nonetheless, all grids achieve a nearly identical limit cycle behavior. The pressure spectra recorded in the time interval 50 ms $< t <$ 60 ms are Fourier transformed in Fig. 4. No difference in the dominant frequencies and amplitudes between the different mesh resolutions is apparent. Even the higher modes of the system are captured similarly. The dominant frequency of 1.9 kHz is in line with the dominant far field frequency measured in the experiment. Further comparisons were performed on the local shock structures and position, which showed good agreement between the fine and medium mesh and minor deviations for the coarse mesh. The comparison is omitted here for brevity. In the simulations discussed in the following, the medium grid with 125 209 cells will be used, as it gives nearly identical results as the fine mesh in both quantities of interest, evolution over time, and acoustic response, indicating that all relevant processes are captured.

5.2 Thin wall model validation

The wall heat flux must be approximated to reproduce the measured temperature rise. Therefore the emissivity ϵ and the heat transfer coefficient α must be estimated. From [28, p. 759], a range of $\alpha \in$ (5 W/(m^{2}K),40 W/(m^{2}K)) is estimated based on the varying tube diameter and thickness. Furthermore, an emissivity $\epsilon \in$ 0.3-0.9 is assumed [6]. In Fig. 5, the temperature signal of the cavity tip is plotted for an adiabatic cavity, the parameters α = 11 W/(m^2 K) and ϵ = 0.75 also used in [6] and a new parameter set α = 7.5 W/(m^2 K) and ϵ = 0.3 used in the remainder of this work. The new parameters were estimated by manual optimisation over consecutive simulations starting from the original set from Bauer [6]. Also indicated is the experimentally measured tip temperature at the limit cycle as dotted line. The adiabatic case does not run into a clear limit cycle behavior as the other simulations. The adiabatic signal is superimposed by low-frequency oscillations. Nonetheless, the adiabatic temperature is capped at roughly 1400 K representing a physical limit based on the disappearance of the shock in the cavity, which can no longer form from collapsing compression waves due to the high temperatures [9]. The parameters α = 11 W/(m^2 K) and ϵ = 0.75 overestimate the heat loss to the walls resulting in an underestimated tip temperature. The parameters α = 7.5 W/(m^2 K) and ϵ = 0.3 result in a better fit to the experimental data. These values were used to fit the limit cycle temperature to the experimental measurement. The chosen values are close to the previously stated physical limit. Especially for the emissivity, this is caused by the simplification $T_{\mathrm{ow}} \approx T_{\mathrm{iw}}$ in the thin wall model leading to overestimated radiation losses. To compensate, a low emissivity is chosen. In the following, the model parameters are kept constant as the chosen parameter set is able to predict the limit cycle temperature for a wide variety of nozzle-tube distances s/d_n.

5.3 Parameter variation

In Fig. 6, the experimentally observed temperature increase (black) is plotted against the nozzle cavity spacing. Also shown are the simulation results (red), all utilizing the same settings for the thin wall model α = 7.5 W/(m^2 K), and

DOI: 10.13009/EUCASS2023-621

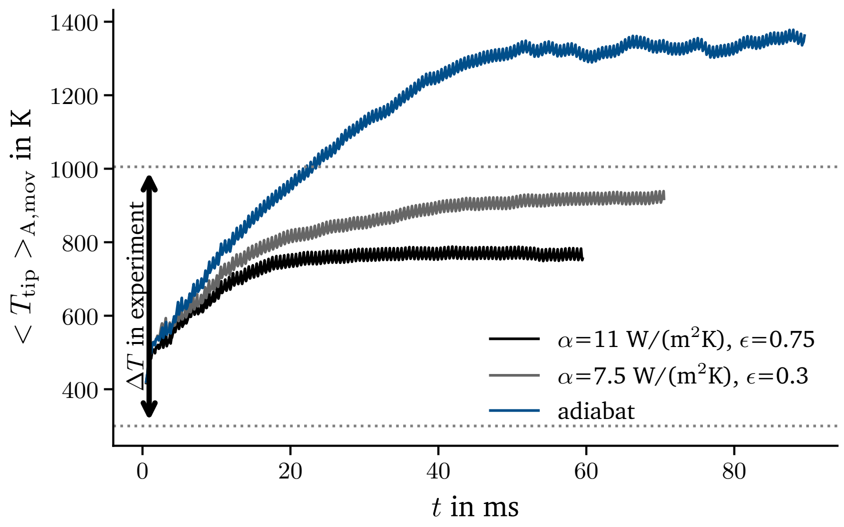

Figure 5: Area-averaged tube tip temperature with a moving average filter for different parameters of the thin-wall model and adiabatic tube walls. Also shown is the experimentally observed temperature as dotted line.

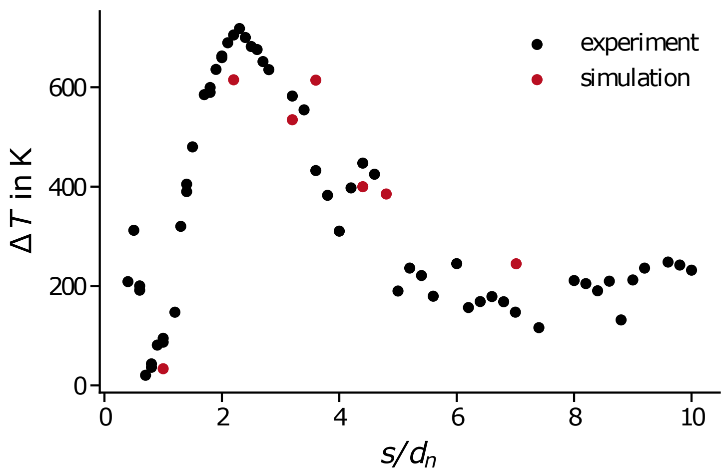

Figure 6: Increase in tube tip temperature with variation of nozzle-tube distance s/d_n in experiments and simulations.

$\epsilon = 0.3$. The highest temperature rise is observed for a $s/d_n = 2.2$. Here the JRM mode is present as the dominant frequency is 1.9 kHz. For smaller nozzle cavity spacing, the ΔT falls drastically. For $s/d_n = 2.2$, the cavity opening is in the so-called *zone of instability* of the underexpanded jet. With the reduction of s/d_n, the cavity is placed ahead of the free stream shock, and no JRM can form. For $s/d_n > 2.2$ ΔT also drops until it reaches a plateau of $\Delta T = 200$ K at $s/d_n = 6$. The simulations are able to reproduce both the peak of ΔT at $s/d_n = 2.2$, for which the thin wall model was fitted, as well as the regions besides the maxima. The simulations are generally within the scatter of the experimental observations. The simulations reproduce both the ΔT gradients as well as the plateau for large s/d_n. In the following, the JRM for $s/d_n = 2.2$ is firstly analyzed as a baseline. Afterwards, the transition to other operating conditions is discussed.

For $s/d_n = 2.2$, the density field in front of the tube entry is shown in Fig. 7 for varying instances over one oscillation in the limit cycle. In addition, the velocity and pressure along the symmetry axis of the tube are shown. During large parts of the outflow phase ($t = 69.28, 69.35, 69.68$ ms), a barrel shock system is present in the density fields, while the shock in the inflow phase ($t = 69.43 - 69.59$ ms) features a diamond shape marked in Fig. 7 by red lines. The studied NPR of 4 lies in the transition region from moderately to highly underexpanded jets [20]. The observed barrel-diamond shift is associated with this transitional NPR. In [15, p. 135], such a transition was also detected for NPR = 3.79 during the JRM.

DOI: 10.13009/EUCASS2023-621

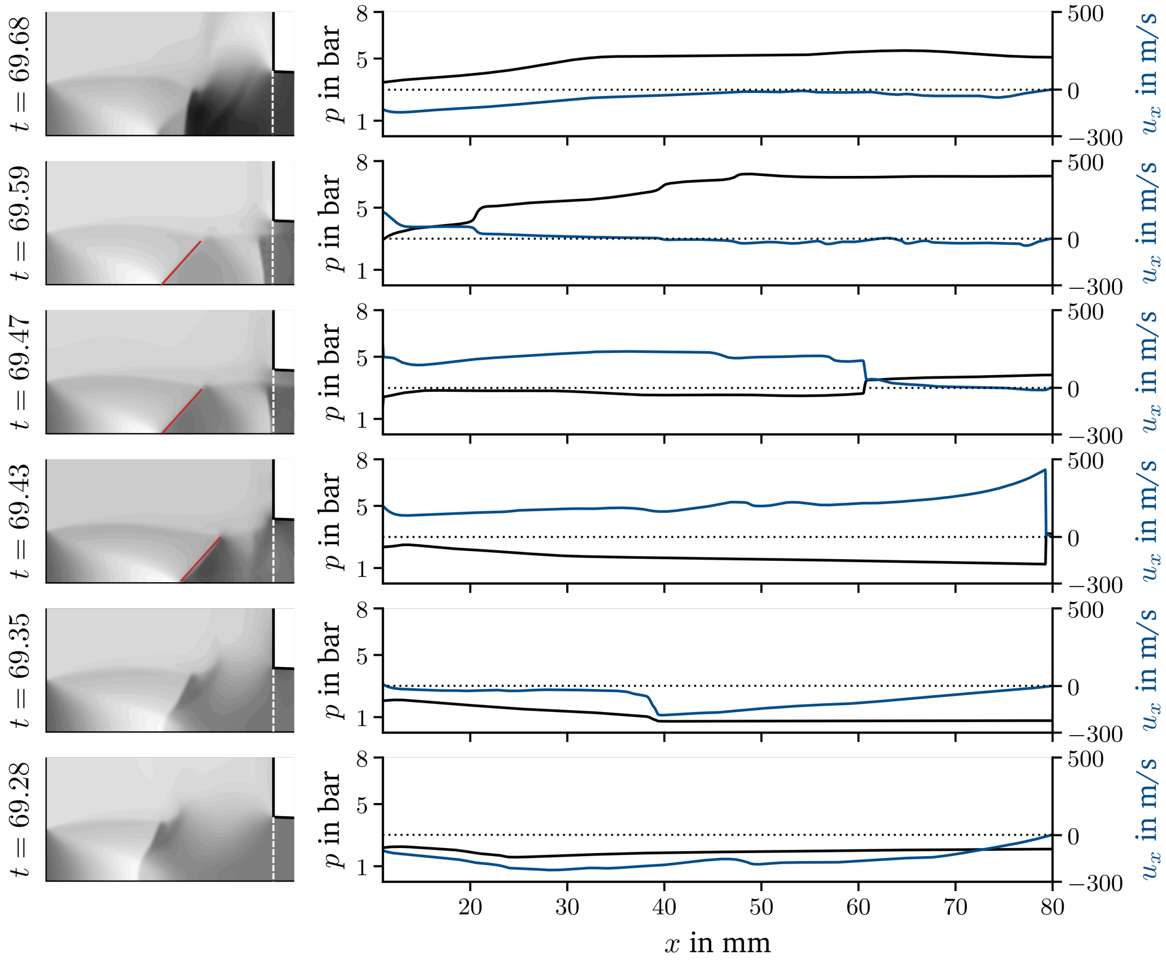

Figure 7: Flow cycle in JRM for $s/d_n = 2.2$, illustrated by the density field between nozzle outlet and tube inlet (left). The diamond shock structure during the inflow cycle is marked with red lines.The axial velocity and pressure in the tube are plotted on the right. The plot starts at the entrance of the cavity, which is marked with a dashed white line in the density field plots on the left. The black dotted line marks zero velocity.

Initially, the tube is in the outflow phase ($t = 69.28$ ms), i.e., the axial velocity in the tube is negative, and the pressure is comparatively low. When the inflow cycle begins ($t = 69.35$ ms), the jet expands because it is no longer pushed towards the nozzle by the outflowing mass of the tube. A shock moves in the tube towards ($x = 40$ mm) the tip and raises the pressure, which is below the ambient pressure. The velocity is negative in the tube area that has not yet been exposed to the shock, while it is approximately zero in the area where the shock has already passed through. The shock passes through the tube and is close to the tip at $t = 69.43$ ms. At this point, the pressure difference across the shock is higher than in the previous time step, i.e., the shock has been amplified over the length of the nozzle. A shock is already forming at the tube inlet, and the length of the first shock cell has reached its maximum. For $t = 69.47$ ms, the shock has already been reflected at the tip and propagates towards the nozzle. The velocity behind the shock is approximately zero, while it is positive before the shock, i.e., the inflow phase is still present. A shock has formed at the entrance of the tube. The velocity in the tube is zero over a wide range. A positive velocity is observed only at the tube entrance for $t = 69.59$ ms. Three areas with high gradients in the pressure mark the positions of shock structures moving through the cavity. The pressure in the tube decreases for $t = 69.68$ ms while the velocity at the tube inlet changes direction, and the shock at the tube inlet is pushed towards the nozzle. The fusion with the diamond shock creates a barrel shock. Now the pressure and velocity in the tube continue to decrease until the outflow phase is completed, and the cycle starts again from the beginning.

Analogous relationships for the direction of velocity and shock movement inside the tube are described in [16, p. 9] for a conical tube. In [15, p. 136], a shock is mentioned, located at the tube inlet during a part of the JRM. The shock is also present at the tube inlet in the phase in which the reflected shock moves from the tube tip to the tube inlet. From a time-distance plot for the problem simulated there, it can be seen that this tube inlet shock moves towards the tube tip and merges with the reflected shock, and this merged shock is then pushed towards the nozzle so that the shock

DOI: 10.13009/EUCASS2023-621

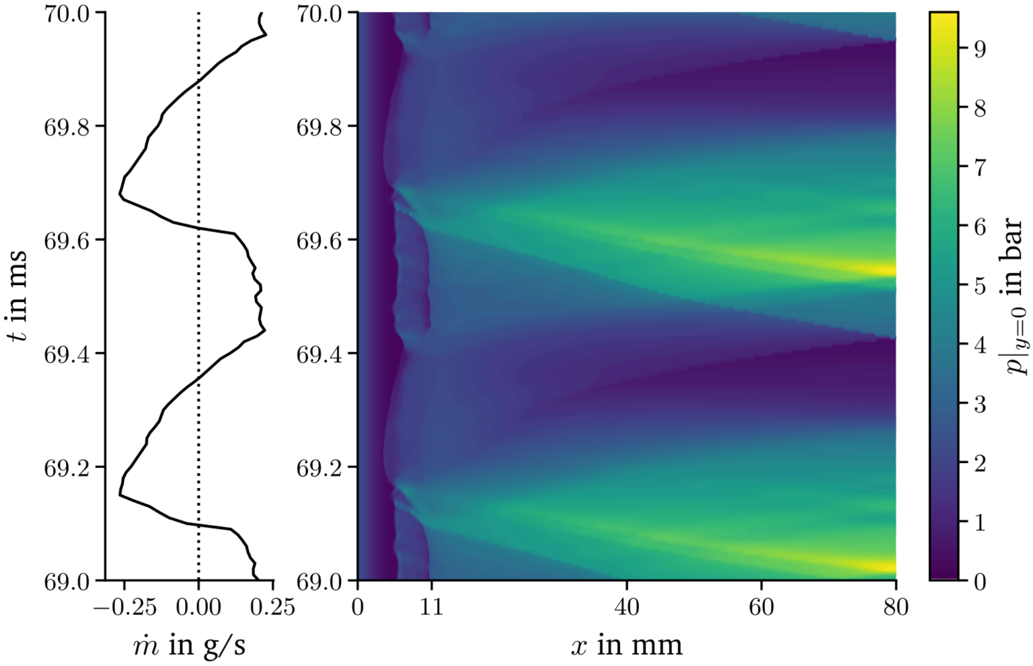

Figure 8: Time-distance diagram generated from the pressure at the symmetry axis of the tube for $s/d_n = 2.2$ (right). For better understanding, the mass flow at the tube inlet is plotted (left).

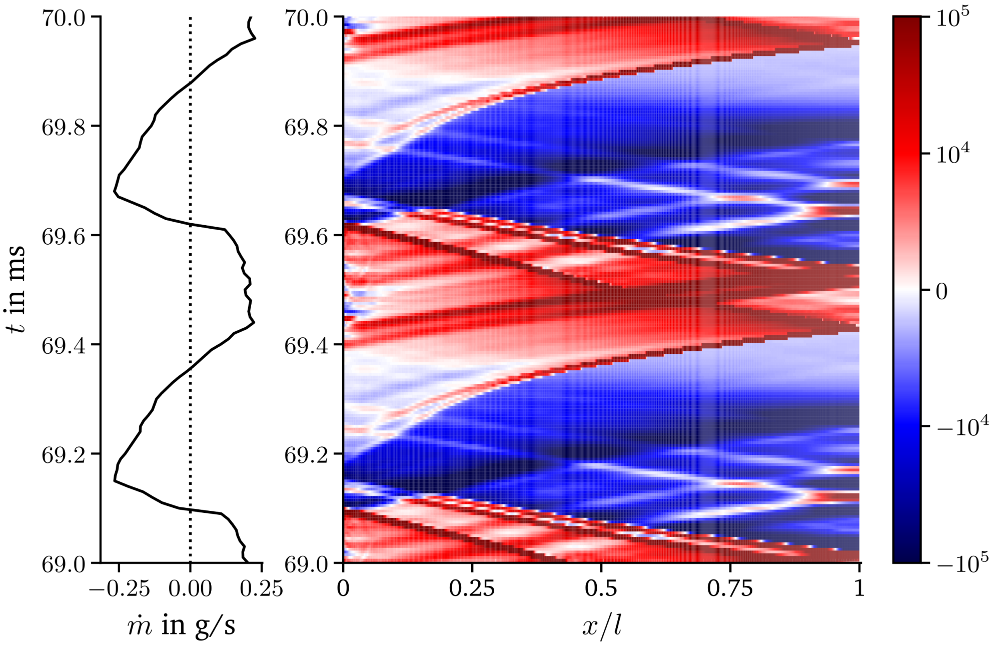

Figure 9: Expansion and compression waves during JRM represented by the time derivative of the pressure along the symmetry axis from tube inlet to tube tip for $s/d_n = 2.2$.

system now only consists of a barrel shock. While the transition to the barrel shock is also visible in this case, the tube inlet shock does not move towards the tube tip, as seen from Fig. 8.

This time-distance diagram is generated by color-coding the pressure along the tube's symmetry axis and using the time domain as the second axis of the diagram. In Fig. 8, the shock in the tube reaching the tip coincide with the diamond shock's maximum expansion (cf. Fig. 7). This is explained by the absence of a mass flow out of the tube. From this diamond shock, an almost normal shock forms at the tube inlet ($x = 11$ mm). This shock is pushed towards

DOI: 10.13009/EUCASS2023-621

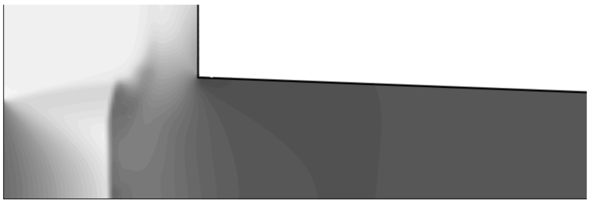

Figure 10: Density field between nozzle exit an the tube's open end for steady state (t = 55 ms) in the case of s/d_n = 1.

the nozzle after the reflected shock has passed the tube inlet due to mass outflow from the tube, seen in Fig. 8. The distinctive pressure discontinuity of the first shock wave of the flow cycle is only recognizable from $x \approx 30$ mm. This indicates the collapse of compression waves due to their different propagation velocities and shock formation.

The coincidence of the compression waves and also the expansion and compression phase of the JRM becomes even clearer if, instead of the pressure along the symmetry axis, the temporal change of the pressure is color-coded in the time-distance diagram. For this purpose, the gradient along the time ordinate is calculated for the data from Fig. 8, which leads to Fig. 9. Here, positive pressure gradients, i.e., areas where the fluid is compressed, are shown in red and expansion regions in blue. Here the expansion fan spreads in the direction of the tube tip from the moment the reflected shock reaches the tube lip. The expansion fan thus arises from the reflection of the shock at the tube inlet. The expansion and compression phases overlap. This overlapping is caused by the conical shape of the cavity as shown in Sec. 5.6. The shock strengthening on the way to the tube tip is visible in Fig. 9.

5.4 Small Nozzle-Tube Spacing

When decreasing the s/d_n ratio to 1, the HS tube is no longer operated in JRM. Neither in the experimental or simulated pressure spectra does the frequency around 2 kHz, characteristic of the JRM mode, dominate. Instead, in the simulation, the HS tube behaves like a flat wall, i.e., there is no mass flow across the tube inlet. In particular, the underexpanded jet and the associated shock structure for the cavity cannot fully form but are squeezed in expansion, as can be seen in Fig. 10, illustrating the nearly steady shock structure in front of the cavity.

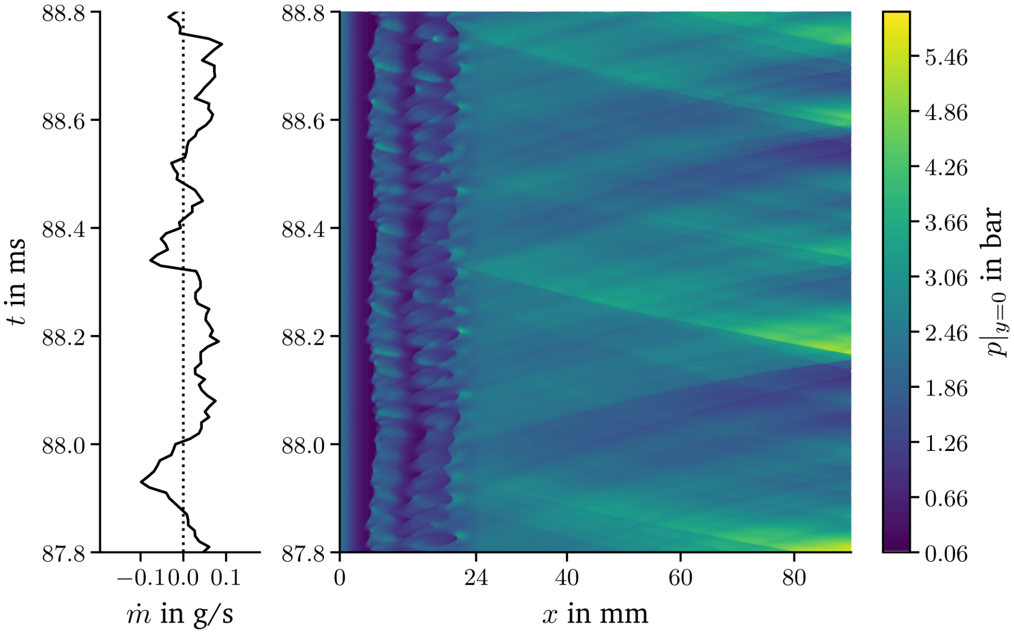

Figure 11: Time-distance diagram generated from the pressure at the symmetry axis for s/d_n = 4.8.

DOI: 10.13009/EUCASS2023-621

5.5 Larger Nozzle Tube Spacing

With an increase in the nozzle tube spacing, the JRM transitions towards a JSM. In Fig. 11, the time distance plot and the mass flow through the cavity inlet are plotted for the $s/d_n = 4.8$. High-frequency oscillations of the screech mode superimpose the inflow and outflow phase of the JRM. Also, the overall mass flux is smaller by a factor of 2.5 compared to the $s/d_n = 2.2$ case. In the time distance plot on the right, compression waves can still be observed in the cavity, but they are much weaker. Furthermore, many overlapping waves are observed. These are caused by the high-frequency oscillation of the shock structure in front of the cavity. These oscillations of the different jet shock cells are visualized in the time distance plot for $x \in [5\,\mathrm{mm}, 24\,\mathrm{mm}]$. Fourier transformation of the time distance plot correlates the oscillation of these shock cells with the high-frequency screech mode at 26.5 kHz. Even though the dominant frequency in the higher frequency range for simulation and experiment do not coincide, both are in the 20 – 30 kHz range. The quarter-wavelength frequency is still recognizable in the simulations. Whereby it is to be noted that this fundamental frequency of the tube has further increased for $s/d_n = 4.8$ from 1.9 kHz at $s/d_n = 2.2$ and 2.3 kHz at $s/d_n = 4.4$. Due to the position of the experimental microphone probe at a much greater distance from the cavity as the computational domain, a direct comparison of the high-frequency noise is not possible and therefore omitted here.

5.6 Influence of cavity shape

To analyze the influence of the conical shape, a cylindrical cavity is simulated for comparison. A lower limit cycle temperature increase of 100 K compared to 600 K for the conical cavity is achieved. To understand the difference again, time-distance plots of pressure and temporal pressure gradient alongside the mass flow into the cavity are shown in Fig. 12 and 13. In the cylindrical case the mass flow features plateau during the outflow. This is in contrast to the conical cavity, where the maximum outflow peak directly transitions again to an inflow. In Fig. 12, there is a clear reflection at the tip in the cylindrical case, while two distinct peaks are visible in the conical case. Similar discrepancies are also visible in Fig. 13. In general, the reached pressures are smaller by a factor of two, explaining also the reduced temperature increase. Afzali et al. [16] suggested that the converging geometry dissipates more energy than in the cylindrical case.

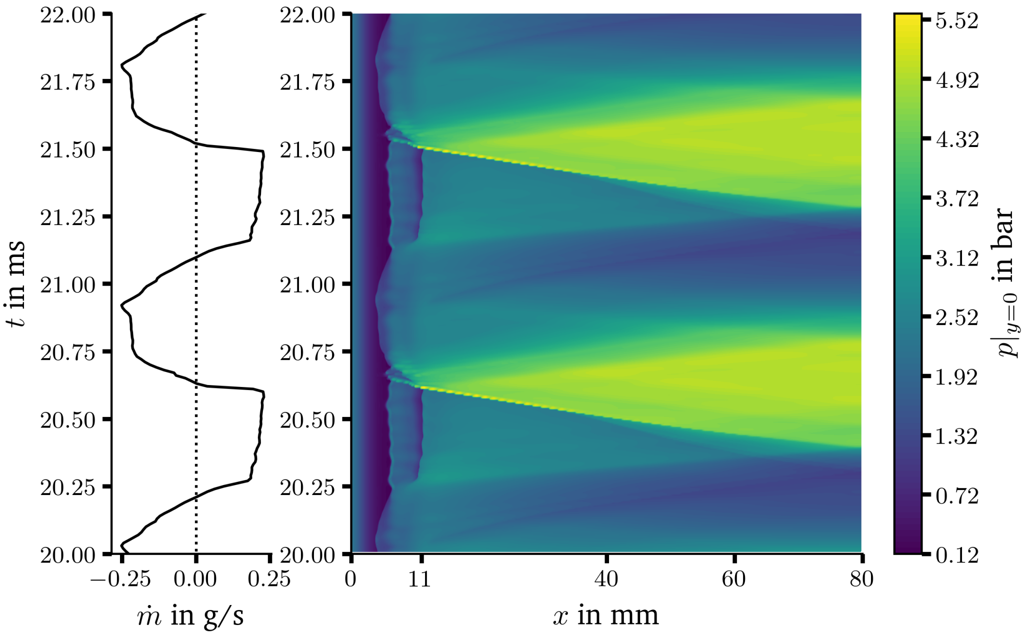

Figure 12: Time-distance diagram generated from the pressure at the symmetry axis of the cylindrical tube for $s/d_n = 2.2$. The mass flow at the tube inlet is shown on the left.

DOI: 10.13009/EUCASS2023-621

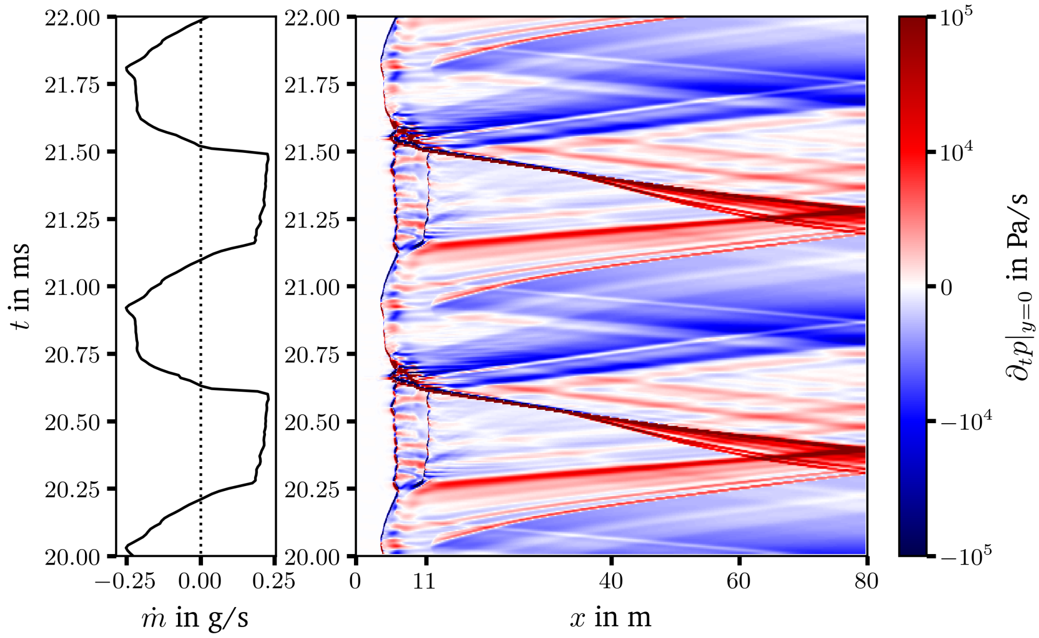

Figure 13: Expansion and compression waves during JRM represented by the time derivative of the pressure along the symmetry axis from the cylindrical tube inlet to tube tip for $s/d_n = 2.2$. The mass flow at the tube inlet is shown on the left.

6. Conclusion

In the presented work, numerical simulations of a resonance igniter configuration have been carried out using the open-source library *blastFoam*. The numerical schemes were verified against literature test cases [26, 27]. Then validation against the experimental data from [17] was carried out. Here the parameters of a wall heat transfer model were calibrated for the geometric configuration with the highest temperature increase. Using the realizable k-ε turbulence model, the simulation predicted a temperature rise of 615 K at the tip, which is $\approx$ 75 K lower than the experimental observations. The trend of the temperature increase as a function of the nozzle-tube distance could be reproduced by the simulations.

The model used to approximate the heat flux around the tube neglects axial heat conduction. The contribution of heat transfer by convection and radiation at the outer wall of the tube is determined by the calibrated parameters. The calibrated heat transfer model was able to reproduce the experimentally obtained temperature rises when the spacing between nozzle outlet and tube inlet was changed.

The change in nozzle-tube distance s/d_n resulted in a transition from the tube operating in jet regurgitant mode (JRM) to the tube operating in jet screech mode (JSM). For some of the s/d_n ratios studied, flow features associated with each of the two modes occurred simultaneously. In addition, the simulation with $s/d_n = 1$ behaves like a flat wall, pressure and temperature oscillations are not present. For the operation in JRM, it was found that the expansion and compression phases, overlap during the flow cycle. The simulation of a cylindrical cavity did not show such overlap. For the geometry studied, the JRM results in higher heating rates than the JSM. This is especially the case when compression waves collapse into a shock. In addition, fluid is trapped at the end of the tube which is continuously compressed and expanded. The cylindrical cavity simulation resulted in much lower temperatures at the tip.

In order to better understand why high heating rates and resonance occur only at distinct s/d_n ratios further research is needed. A change in the tube inlet geometry could provide new insights, as it is known that these influence the operation mode of the tube [6, p. 93]. However, little validation data exist for the effect of cavity inlet geometry. As first step the effect of cavity lip-thickness for a sharp cornered cavity could be studied. In the final applications heat-losses to the wall are most likely absorbed by the ignitable mixture again. Therefore studies of functional igniters should consider conjugated heat transfer calculations. Future studies will leverage the validated numerical solver to optimize and study small-scale igniters for cubesat applications, where heat-losses are even more important [29].

7. Acknowledgments

J. Karpowski, F. Ferraro and C. Hasse thank the "Bundesminesterium für Bildung und Forschung" for the recieved funding through the project CFD4H2.

References

[1] Statista. Number of active satellites by year. *www.statista.com/statistics/897719/number-of-active-satellites-by-year/*, 2023.

[2] Paul LUNGU, Christian BAUER, and Oskar J. HAIDN. Design aspects and characterisation of a resonance igniter for oxygen/methane in-orbit propulsion systems. *Proceedings of the 8th European Conference for Aeronautics and Space Sciences. Madrid, Spain, 1-4 july 2019*, 2019.

[3] William Conrad and Albert J. Pavi. A resonance-tube igniter for hydrogen-oxygen rocket engines. Technical report, NASA Lewis Research Center Cleveland, OH, United States, 1967.

[4] Bert R. Phillips and Albert J. Pavi. Resonance tube ignition of hydrogen-oxygen mixtures. Technical report, NASA Lewis Research Center Cleveland, OH, United States, 1971.

[5] Zoe Dickert. Gox-ethanol resonance ignition system design: Design and modeling of the gas dynamic heating in a gox-ethanol resonance ignition device. Master's thesis, Delft University of Technology, 2020.

[6] Christian Bauer. *Design and Test of Resonance Ignition Systems for Methane/Oxygen In-Space Propulsion Systems*. PhD thesis, Technische Universität München, 2020.

[7] Ganesh Raman and K. Srinivasan. The powered resonance tube: From Hartmann's discovery to current active flow control applications. *Progress in Aerospace Sciences*, 45(4-5):97–123, 2009.

[8] Virendra Sarohia and Lloyd H. Back. Experimental investigation of flow and heating in a resonance tube. *Journal of Fluid Mechanics*, 94(4):649672, 1979.

[9] E. Brocher and C. Maresca. Study of thermal phenomena in a Hartmann-Sprenger tube. *International Journal of Heat and Mass Transfer*, 16:529–548, 1973.

[10] Timothy J. N. Smith and Alan Powell. Experiments concerning the hartmann whistle. 1964.

[11] J. Iwamoto. Experimental study of flow oscillation in a rectangular jet-driven tube. *Journal of Fluids Engineering*, 112(1):23–27, 1990.

[12] Andrea Romano. Verification and validation of a cfd simulation model for resonance igniter heat-up phase. Master's thesis, Politecnico di Torino, 2019.

[13] S. Murugappan and E. Gutmark. Parametric study of the hartmann–sprenger tube. *Experiments in Fluids*, 38(6):813–823, 2005.

[14] B R Vinoth, P Throvagunta, and E Rathakrishnan. Effect of tube lip thickness on the performance of hartmann–sprenger tubes. *Proceedings of the Institution of Mechanical Engineers, Part G: Journal of Aerospace Engineering*, 226(1):74–87, 2011.

[15] MG Lebedev and OV Bocharova. Self-oscillatory flow in the hartmann resonator – numerical simulation. *International Journal of Aeroacoustics*, 19(1-2):119–154, 2020.

[16] Babak Afzali and Hassan Karimi. Numerical investigation on thermo-acoustic effects and flow characteristics in semi-conical Hartmann–Sprenger resonance tube. *Proceedings of the Institution of Mechanical Engineers, Part G: Journal of Aerospace Engineering*, 231(14):2706–2722, sep 2016.

[17] Christian Bauer, Paul Lungu, and Oskar J. Haidn. Numerical and Experimental Investigations on Resonance Ignition. In *Space Propulsion Conference*, 2014.

[18] Frank White. *Viscous Fluid Flow*. McGraw-Hill Education, 2005.

[19] Tsan-Hsing Shih, William W. Liou, Aamir Shabbir, Zhigang Yang, and Jiang Zhu. A new k- eddy viscosity model for high reynolds number turbulent flows. *Computers & Fluids*, 24(3):227–238, 1995.

DOI: 10.13009/EUCASS2023-621

[20] Erwin Franquet, Vincent Perrier, Stéphane Gibout, and Pascal Bruel. Free underexpanded jets in a quiescentmedium: A Review, 2015.

[21] Bram Van Leer. Towards the ultimate conservative difference scheme. V. A second-order sequel to Godunov's method. *Journal of Computational Physics*, 32(1):101–136, July 1979.

[22] P L Roe. Characteristic-Based Schemes for the Euler Equations. *Annu. Rev. Fluid Mech.*, 18(1):337–365, January 1986.

[23] Eleuterio F. Toro. *Riemann Solvers and Numerical Methods for Fluid Dynamics*. Springer, 2009.

[24] blastFoam: A solver for compressible multi-fluid flow with application to high-explosive detonation.

[25] Gary A Sod. A survey of several finite difference methods for systems of nonlinear hyperbolic conservation laws. *Journal of Computational Physics*, 27(1):1–31, 1978.

[26] Peter D. Lax and Xu-Dong Liu. Solution of two-dimensional riemann problems of gas dynamics by positive schemes. *SIAM Journal on Scientific Computing*, 19(2):319–340, 1998.

[27] Paul Woodward and Phillip Colella. The numerical simulation of two-dimensional fluid flow with strong shocks. *Journal of Computational Physics*, 54(1):115–173, 1984.

[28] VDI-Gesellschaft Verfahrenstechnik und Chemieingenieurwesen, editor. *VDI-Wärmeatlas*. Springer-Verlag, 2013.

[29] Henrike Jakob, Justus Albert, and Heinz-Peter Schiffer. Research and test activities on sustainable space propulsion systems at TU Darmstadt. *Proceedings of the 10th European Conference for Aeronautics and Space Sciences. Lausanne, Switzerland (accepted)*, 2023.